J Solid State Electrochem (2017) 21:2975–2984
DOI 10.1007/s10008-017-3617-0

ORIGINAL PAPER

Biomass-derived porous carbon electrode modified with nanostructured nickel-cobalt hydroxide for high-performance supercapacitors

Jie Zhang[1] · Jinwei Chen[1] · Haowei Yang[1] · Jinlong Fan[1] · Feilong Zhou[1] · Yichun Wang[1] · Gang Wang[1] · Ruilin Wang[1]

Received: 20 February 2017 / Revised: 19 April 2017 / Accepted: 23 April 2017 / Published online: 18 May 2017

Abstract Apple-derived porous carbon (denoted as APC) is successfully prepared and analyzed as a potential carbon material by hydrothermal carbonization and pyrolysis, which exhibits a high specific surface area and porous structure. Furthermore, nickel–cobalt double hydroxide (Ni–Co DH) is synthesized by design of hybrid nanowires on APC for supercapacitors via a simple hydrothermal process. The fabricated electrode produces a capacitance of 1519 F g^{-1} at 1 A g^{-1}, and 90.2% of the capacitance is retained after 2000 cycles at a high current density. An asymmetric supercapacitor (ASC) is assembled using the Ni–Co DH@APC as the positive electrode and active carbon as the negative electrode. The ASC exhibits a prominent energy density of 61.2 Wh kg^{-1} and high power density of 14,400 W kg^{-1} at 5 A g^{-1}. The desirable electrochemical performance can be attributed to the suitability of APC as a support and the Ni–Co nanostructure constructed on the surface of APC as an effective active material for high-energy and long-life cycling supercapacitor applications. The fabricated composite provides a potential design of low-cost functional carbon materials that can be produced in large scale by using biomass as starting materials.

Keywords Porous carbon · Nickel–cobalt double hydroxides · Supercapacitor · Electrode material · High performance

Electronic supplementary material The online version of this article (doi:10.1007/s10008-017-3617-0) contains supplementary material, which is available to authorized users.

✉ Jinwei Chen
jwchen@scu.edu.cn

[1] College of Materials Science and Engineering, Sichuan University, Chengdu 610065, People's Republic of China

Introduction

Supercapacitors, which possess high power density, fast charge–discharge rate, and long life cycles and are environment friendly, gained substantial attention in the field of energy storage in recent years [1]. Up to now, tremendous efforts were devoted to develop electrode materials for capacitors, including research on conductive polymers, such as polyaniline or polypyrrole, and transition metal oxides or hydroxides, such as MnO_2, RuO_2, NiO, $Ni(OH)_2$, Co_3O_4, V_2O_5, and FeOOH [2–12]. Among the various active materials, Ni- and Co-based materials are potential candidates because of their low cost, low toxicity, and abundant reserve [13]. These materials have high specific capacitances but are limited by poor electric conductivity and cycling stability, resulting in rapid loss of capacity. To overcome these obstacles, double hydroxides (DHs), such as Ni–Co DH, exhibit high conductivity, rich redox ability, increased capacitance, and considerable cycle stability unlike pure $Ni(OH)_2$. However, many issues exist because of the inferior supercapacitor performance of pristine DH materials induced by their relatively poor electron conductivity and low mass diffusion. A new tendency was presented on hybrid capacitors, which apply nanostructured carbon as conductive agent and metal hydroxides as active materials and improve the high specific surface area, electrical conductivity, and the electrochemical performance [14].

Among various carbons, porous carbon is a common material for catalyst support and supercapacitors. In supercapacitors, carbons with high surface area and porosity have widely been used due to their excellent cycling stability, safe operation, high power density, and stable physicochemical properties [15, 16]. Zhou et al. reported NiCo binary hydroxide nanosheets and titanium carbide–carbon nanofiber with high specific capacitance of 2224 F g^{-1} and excellent cyclic stability [17]. Chang et al. synthesized $Co(OH)_2/Ni(OH)_2$ nanomaterials loaded on conducting carbon fiber paper with a higher cycling stability (92.4% specific

capacitance remains) over 20,000 charge–discharge cycles [18]. Therefore, it is significant to choose an advisable type of carbon material to overcome the aggregation and poor electrical conductivity of Ni–Co DH. Much research on porous carbon materials was conducted by extracting fossil fuel sources under relatively harsh conditions, which involve toxic organics, high temperature, complicated steps, and uncontrollable factors and significantly affect the environment [19]. Low-cost, sustainable, and environmentally benign electrode materials derived from biomass materials have caused widespread concern over the recent years. Apple is a common fruit because of its abundance worldwide and availability in any season. The heterogeneous structure of apple includes carbohydrates, pectins, nicotinic acid, free sugars, proteins, and crystalline cellulose. Most of the components above favor the formation of carbon at appropriate pyrolysis temperatures [20]. Various biomass-derived porous carbon materials, such as from cocoon silk, crab shell corn, shiitake mushroom, celtuce leaves, and ginkgo shells, were reported [21]. These materials are applied as electrode materials for sensors, supercapacitors, and Li-ion batteries. Thus, biomass-derived porous carbon can be potentially applied in energy storage.

Thus, we adopted a simple hydrothermal carbonization process to prepare porous carbon. A Ni–Co DH, which was constructed using nanowires covered on apple-derived porous carbon (APC), was prepared by a facial hydrothermal method for supercapacitors where APC acted as support to disperse the Ni–Co DH. This unique structure provides sufficient channels for the access of electrolyte, the high utilization rate of electrode materials, and high electrical conductivity. Electrochemical measurements demonstrated that the Ni_2Co_1 DH@APC exhibited high Csp (approximately 1519 F g^{-1} at 1 A g^{-1}) and excellent cycling stability. The asymmetric supercapacitor (ASC) exhibits a prominent energy density of 61.2 Wh kg^{-1} and high power density of 14,400 W kg^{-1} at 5 A g^{-1}.

Experimental

Preparation of APC

The carbonaceous precursor was prepared by a simple hydrothermal reaction. Fresh apples, which were obtained from a market, were cut into pieces, and 1 g apple sheets were placed into a Teflon-lined stainless steel autoclave without any solvent. The autoclave was heated in an oven at 180 °C for 12 h to achieve the brown carbonaceous product. The product was cleaned in deionized water and 1 M KOH solution, boiled for 2 h to remove the soluble impurities, and dried in a vacuum oven at 80 °C for 8 h. As-prepared carbonaceous precursor was mixed with KOH powder at a mass ratio of 1:4. The mixture was heated to 700 °C for 2 h in a tube furnace under Ar protection to obtain a black resultant. The as-formed carbon materials were washed in 2 M HCl at 50 °C for 4 h to remove the residual KOH. The resulting product was washed again and dried overnight. For comparison, the products without KOH activation were also prepared by employing the same method.

Fabrication of Ni–Co DH nanowires

Different molar ratios of $Ni(NO_3)_2$ and $Co(NO_3)_2$ were used to synthesize Ni–Co DH. For example, 182 mg of $Co(NO_3)_2 \cdot 6H_2O$ and 90 mg of $Ni(NO_3)_2 \cdot 6H_2O$ were dissolved in 40 mL deionized water, and 600 mg urea and 50 mg APC powders were added to synthesize 60 wt% Ni_2Co_1 DH@APC. The mixed solution was transferred into a Teflon-lined stainless steel autoclave and maintained at 180 °C for 10 h. After cooling the solution to room temperature, the sample was washed with deionized water and dried at 80 °C overnight. For comparison, the DH composites with different Ni/Co molar ratios were also prepared under the same condition. All the samples preserved the mass ratio of 60 wt% hydroxides in the composites.

Material characterization

To investigate the structure and composition of the samples, powder X-ray diffraction (XRD, DX-2700, Dandong) was performed using Cu Kα radiation. The Brunauer–Emmett–Teller (BET) specific surface area and pore size were determined by nitrogen adsorption or desorption measurement. The morphologies of the samples were characterized by scanning electron microscopy (SEM, JSM-5900LV, JEOL Co.) and transmission electron microscopy (TEM, Carl Zeiss SMT, Libra 200FE). Thermal gravimetric analysis (TGA) was performed on STA 2500 (NETZSCH, Germany). The chemical composition of the Ni–Co DH@APC was characterized by energy-dispersive X-ray spectroscopy (EDS, INCA 300) and X-ray photoelectron spectroscopy (XPS, Kratos AXIS ULTRA).

Electrochemical measurement

The cyclic voltammetry (CV), galvanostatic charge or discharge, and electrochemical impedance spectroscopy (EIS) measurements were conducted out in a 6-M KOH solution with an Autolab PGSTAT302N (Metrohm Autolab, The Netherlands) with a three-electrode system. Nickel foam was cut into 10 mm × 10 mm portions and cleaned before being used as a substrate for the working electrode. Hg/HgO electrode was used as the reference electrode, and a carbon plate was utilized as the counter electrode, respectively. The working electrode was prepared by mixing the active material, acetylene black (conductive additive), and polytetrafluoroethylene emulsion (PTFE, 60 wt%) at a weight

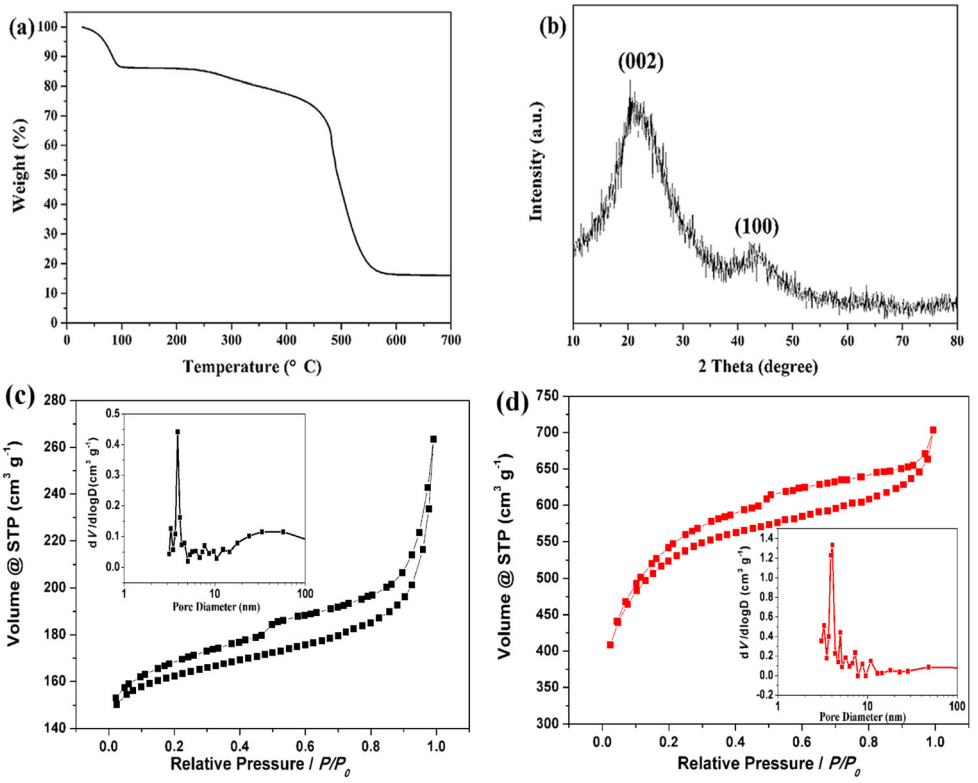

Fig. 1 **a** TG curve of carbonaceous precursor after HTC process, **b** XRD pattern of APC, **c** N_2 adsorption–desorption isotherms and BJH pore size distribution (*inset*) of APC without KOH activation, and **d** APC prepared via KOH activation

ratio of 85:5:5 in ethanol. The mixture was ultrasonically stirred for 30 min to obtain a homogeneous slurry. The moderate slurry was repeatedly extracted by a pipettor, dropped onto the nickel foam, and dried at 80 °C for 6 h. The loading content of the active material was maintained at 1–2 mg cm^{-2} in each electrode. The specific capacitance (C_{sp}, F g^{-1}) can be calculated from the CV curve by adopting Eq. (1),

$$C_s = \int I\mathrm{d}V \Big/ mv\mathrm{d}V \tag{1}$$

where dV is the potential window (V), m is the mass of active materials in the electrodes, and v means scan rate. The gravimetric specific capacitance can also be calculated based on the galvanostatic charge or discharge curves, as indicated in Eq. (2):

$$C = I\Delta t \Big/ (m\Delta V) \tag{2}$$

where m is the mass of active material, I is current density of discharge, Δt represents time of discharge, and ΔV is the potential window. Electrochemical impedance spectroscopy (EIS) measurement was carried out in a frequency range of 0.01–10^6 Hz with amplitude of 5 mV.

The ASCs based on as-prepared Ni–Co DH@APC and active carbon (AC) were fabricated in a two-electrode cell, where Ni–Co DH@APC served as the positive electrode and AC as the negative electrode with electrolyte. The energy densities (E, Wh kg^{-1}) and power densities (P, W kg^{-1}) can be obtained by Eq. (3) and Eq. (4),

$$E = \left(1 \Big/ 2\right) C_{sp} V^2 \tag{3}$$

$$P = 3600\, E \Big/ t \tag{4}$$

where C_{sp} (F g^{-1}) is the specific capacitance of the supercapacitor, t is the discharging time, and V is the cell voltage for charging and discharging excluding the IR drop.

Results and discussion

Characterizations of APC

TGA was performed on the carbonaceous precursor after the HTC process. Figure 1a shows that the first step, which was conducted at around 100 °C, is related to the loss of adsorbed water. The next step (100–450 °C) is correlated with the decomposition of carbohydrates. The main weight loss occurs at approximately 450–500 °C, which is attributed to the conversion of volatile organic species to carbon. The last step (above 700 °C) shows that the sample is gradually stabilized, indicating the formation of carbon. After pyrolysis, the residual mass

of roughly 16% indicates the yield of the type of biomass-derived carbon. The XRD pattern of APC (Fig. 1b) shows two broad diffraction peaks at 21.7° and 43.3°, which correspond to the (002) and (100) diffractions of amorphous carbon. The synergistic effect between the large surface area and good electrical conductivity in electrode materials can significantly enhance the electrochemical property of supercapacitors [22]. The BET surface area and the BJH pore size distribution of the samples are presented in Table S1, indicating that the porous structure of our sample provides efficient transport pathways inside, which plays a dominant role on high-rate applications. Porous carbon without KOH activation (as shown in Fig. 1c) was directly obtained by simple thermal treatment with a surface area of 498 $m^2 g^{-1}$. Types of pores can be divided into micropores ($d < 2$ nm), mesopores ($d = 2$–50 nm), and macropores ($d > 50$ nm) [23]. This type of porous carbon possesses an average pore size of 3.88 nm. The APC prepared via KOH activation (Fig. 1d) has a higher surface area of 1680 $m^2 g^{-1}$. A decomposition reaction occurred with the presence of KOH, involving two processes: 6 KOH + 2 C → 2 K + $3H_2$ + $2K_2CO_3$ and the decomposition of K_2CO_3 and/or reactions of $K/K_2CO_3/CO_2$ with the carbon [21, 24]. As gas escaped, a large amount of nanoscale pores was generated. Several researchers determined that the activated carbons increase the amount of mesopores, which facilitates the mass diffusion in electrodes during an electrochemical reaction [25, 26]. Figure 2a presents an overview of the carbon material with a sponge-like nanostructure. The TEM image indicates that the porous nanoparticles interconnected together, which facilitates ion and electron transport (Fig. 2b).

Characterizations of Ni–Co DH@APC

APC, which was used as a support to synthesize Ni/Co/NiCo hydroxide composites, was specifically investigated. The XRD pattern of the Ni–Co DH@APC is presented in Fig. 3, and it confirms the presence of crystalline $Co(OH)_2$ and $Ni(OH)_2$. For the Ni–Co DH@APC with a Ni/Co molar ratio of 2:1, three main characteristic peaks appear at 11.9°, 34.1°, and 60.3°, which corresponded to the (003), (101), and (110) crystalline facets of α-$Ni(OH)_2$ (referred to as JCPDS no. 38-0715). These peaks indicate that the crystalline α-$Ni(OH)_2$ particles are dominant in the composite. For a Ni/Co molar ratio of 1:2, the diffraction peaks at 33.4° and 38.1° are the characteristic peaks of the $Co(OH)_2$ phase (referred to as JCPDS no. 51-1731). Distinguishing $Ni(OH)_2$ and $Co(OH)_2$ phase is difficult because of the similar structures and the approximated diffraction peaks of these phases. TG analysis of 60 wt% Ni–Co DH@APC was adopted to estimate the transformation of hydroxides and the APC weight percentages of the composites, as shown in Fig. S1. Weight was reduced at around 100 °C because of the removal of physically adsorbed water molecules. The second stage from 100 to 350 °C occurred because of the transformation of hydroxides to oxides [27]. No weight loss occurred when the temperature exceeds 450 °C, indicating the complete removal of APC and the presence of Ni/Co-containing oxides. The calculated weight ratio is close to 60%, which corresponded to its prospective mass fraction. The Ni:Co atomic ratio in Ni–Co DH@APC is determined to be 1:1, 1:2, and 2:1 by EDS, as shown from Fig. S2. As shown in Fig. S3, $Co(OH)_2$ and Ni_2Co_1 DH were grown to be needle-like nanowires by hydrothermal process. The SEM images of the prepared Ni_2Co_1 DH@APC are presented in Fig. 4a, b, which show that the nanowires tightly adhered to APC. The SEM image of APC indicates that the nanowires grew on the surface of APC after the hydrothermal reaction. However, the NiCo nanowires can serve as a direct electroconductive pathway to enhance the transfer of electrons and APC provides a large surface area for the attachment of the Ni–Co DH nanowires. Figure 4c shows the TEM image of the composite, which reveals the Ni–Co DH nanowires are intimately attached to the surface of APC and the fabrication reduces the transport resistance between the active material and carbon support. The schematic of Fig. 4d shows that Ni–Co DH nanowires provide a conductive network for electron transport and more active sites exposed in the electrolyte. On the other hand, APC acts as a support with a large surface area for loading the Ni–Co DH nanowires. The survey spectrum of Ni_2Co_1 DH@APC (Fig. 5a) shows that the formed materials are mainly composed of Ni, Co, C, and O. The main

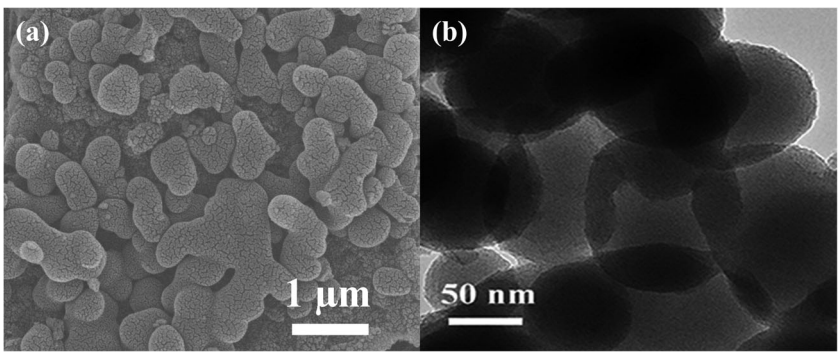

Fig. 2 **a** SEM image of APC and **b** TEM image of APC

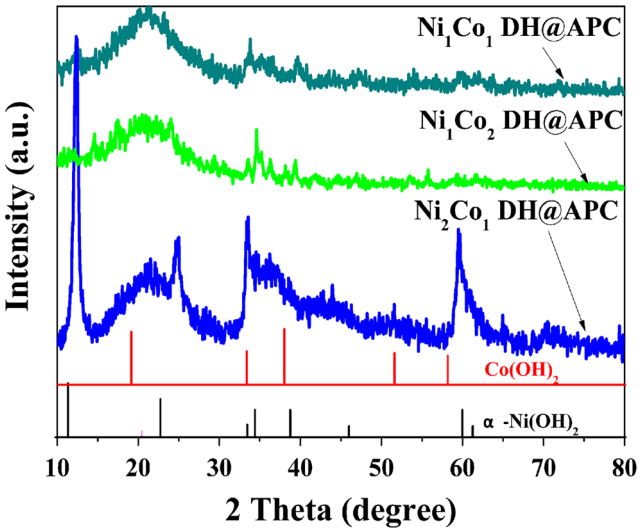

Fig. 3 XRD patterns of Ni–Co DH electrodes with different Ni:Co molar ratios

peak of the O 1s spectrum was located at around 531.1 eV, which is attributed to hydroxide groups (OH^-). The Ni 2p spectrum (Fig. 5b) was fitted considering the two peaks at 873.5 eV in 2p1/2 and 855.9 eV in 2p3/2, which correspond to Ni^{2+} in Ni hydroxides [28, 29]. The Co 2p spectrum (Fig. 5c) was also deconvoluted into two peaks both assigned to Co^{2+}, which indicate that the element Co exists in the $Co(OH)_2$ state [30]. The deconvoluted C 1s spectrum (Fig. 5d) confirms the presence of oxygen-containing functional groups, such as C–C, C–O, and O=C. These groups on the surface of APC play a key role in fabricating the Ni–Co DH@APC nanocomposite. The observed binding energy values of the Ni, Co, O, and C atoms are consistent with that in the literature, which indicate the formation of Ni–Co DH.

Figure 6a shows CVs of the Ni–Co DH electrode with different Ni:Co molar ratios of 1:0, 1:1, 1:2, 2:1, and 0:1 were recorded at the scan rate of 5 mV s^{-1}, indicating that the Ni–Co DH@APC electrodes possessed a significantly higher specific capacitance (according to the comparison of areas) than that of individual $Ni(OH)_2$ or $Co(OH)_2$ electrodes. The pure $Ni(OH)_2$ exhibited a pair of high and well-defined redox peaks in the potential range from 0.25 V (vs. Hg/HgO) to 0.45 V. Pure $Co(OH)_2$ showed a couple of small redox peaks at the potential range of 0.10 to 0.30 V. The redox peaks shifted to a positive potential and broadened with increased $Co(OH)_2$ contents, which indicates improved capacitance. This result can be attributed to the redox potential of $Ni(OH)_2$ to NiOOH, which is more positive than that of $Co(OH)_2$ to CoOOH. In Fig. 6b, the capacitance of the individual Ni_2Co_1 DH electrode is lower than that of Ni_2Co_1 DH@APC. It can be concluded that APC in this composite acts as an electroconductive support to connect and extremely disperse the DH nanowires. The discharge curves were also obtained at different current densities of 1, 2, 5, and 10 A g^{-1}, as shown in Fig. S4. Especially, Fig. 6c shows that the CVs obtained from Ni_2Co_1 DH@APC exhibit a pair of symmetrical cathodic and anodic peaks, indicating the favorable reversibility of the oxidation and reduction processes and good pseudocapacitance behaviors of $Co(OH)_2$ and $Ni(OH)_2$. The two pairs of redox peaks also

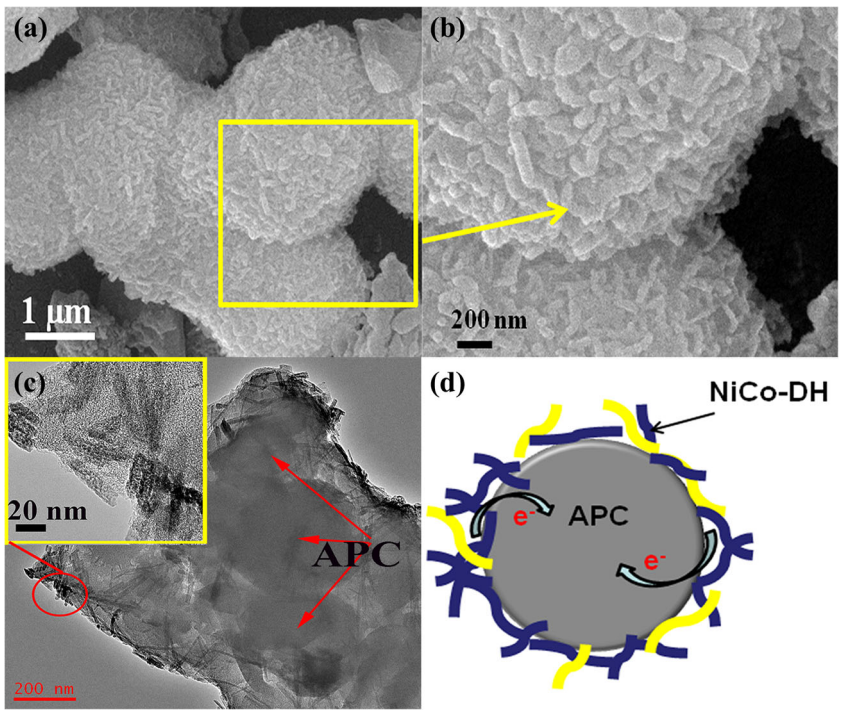

Fig. 4 **a**, **b** SEM images of Ni_2Co_1 DH@APC with different magnifications, **c** TEM images of Ni_2Co_1 DH@APC, and **d** schematic illustration of the electrical pathway in Ni–Co DH nanowires supported on APC

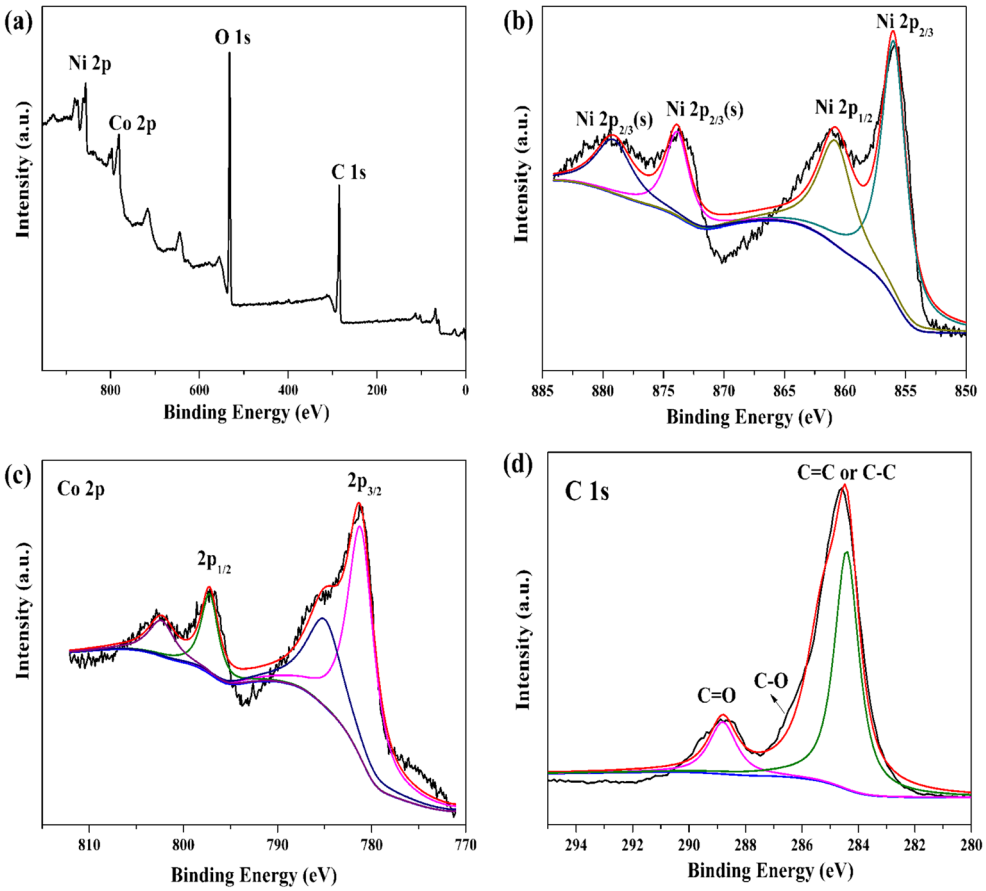

Fig. 5 **a** XPS survey, **b** XPS peaks of Ni 2p, **c** XPS peaks of Co 2p, and **d** XPS peaks of C 1s of Ni_2Co_1 DH@APC

show that the capacitance is mainly determined by faradaic reactions, corresponding to the following mixed reactions in Eqs. (5)–(7) [31, 32]:

$$Ni(OH)_2 + OH^- \rightarrow NiOOH + H_2O + e^- \quad (5)$$

$$Co(OH)_2 + OH^- \rightarrow CoOOH + H_2O + e^- \quad (6)$$

$$CoOOH + OH^- \rightarrow CoO_2 + H_2O + e^- \quad (7)$$

At a scan rate of 20 mV s^{-1} (marked with the red line in Fig. 6c), $Co(OH)_2$ was first oxidized to CoOOH at roughly 0.32 V before the oxidation of $Ni(OH)_2$ to NiOOH (near 0.38 V). Furthermore, a higher theoretical C_{sp} was obtained because the CoOOH is oxidized to CoO_2 around the potential of Ni^{2+}/Ni^{3+} [33]. Figure 6d shows that the charge or discharge curves exhibit a nonlinear charge–discharge feature from the redox reaction, which also confirms the pseudocapacitance behavior because the quasi-reversible redox reactions occurred at the interface between the electrode and electrolyte. Discharge time reduced with increased charge current density because of the low diffusion or migration of charges through the electrodes at higher current densities. At the discharge current densities of 1, 2, 5, and 10 A g^{-1}, the C_{sp} of the Ni_2Co_1 DH@APC electrodes were approximately 1519, 1454, 1411, and 1357 F g^{-1}, respectively. Figure 6e shows the specific capacitance of all the electrodes at different current densities, which is calculated by the discharge CVs from Fig. S4. Ni_2Co_1 DH@APC exhibits better C_{sp} values at all the current densities compared to that of other electrodes, which implies the better charge storage performance of this electrode than that of other electrodes. The increased C_{sp} is also better than that in other reports presented in Table 1. The prolonged discharge time from the sample prepared by the given molar ratio is probably attributed to the multiple phases existing at the intermediate Ni/Co ratios and the broadened redox properties [34]. The mechanism of this untrivial synergetic effect originated from the given Ni/Co ratio can be explained as follows: (i) the Ni–Co DH phase possess the layered crystal structure with broadened interlayer spacing, which can facilitate the ion diffusion within active materials; (ii) as shown in Fig. S3, the length of Ni–Co DHs is shorter than that of $Co(OH)_2$, indicating that the electrolyte could easily access active sites; (iii) the Ni–Co DH structure can improve the electron transportation from active materials to the current collector.

The EIS measurement result was fitted based on an equivalent circuit, and the resulting Nyquist plot is shown in Fig. 6f. The Ni_2Co_1 DH@APC electrode shows a substantially smaller charge transfer resistance (R_{ct}, 0.72 Ω cm^{-2}) compared with that of Ni_2Co_1 DH, indicating that the APC can evidently reduce charge transfer resistance, thus improving the transport

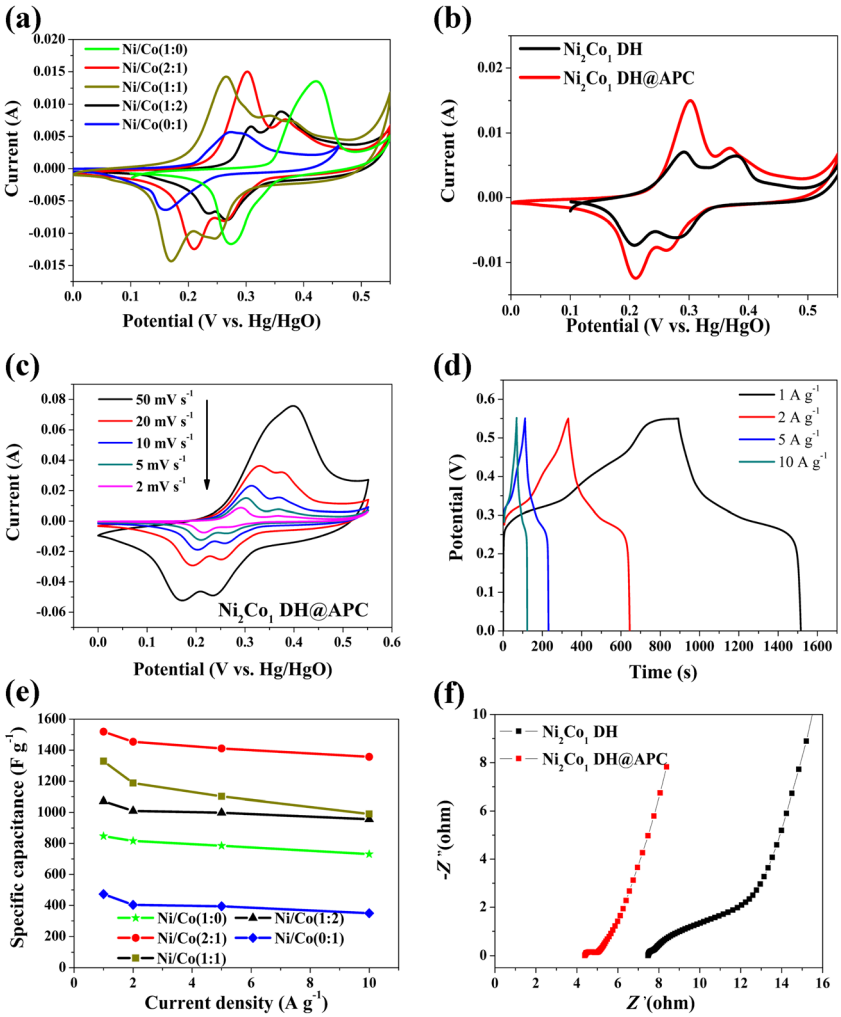

Fig. 6 **a** CV curves of Ni–Co DHs prepared with different Ni:Co molar ratios at a scan rate of 5 mV s^{-1} in 6 M KOH; **b** CV curves of Ni_2Co_1 DH with and without APC as support; **c** CV curves of Ni_2Co_1 DH@APC electrode at different scan rates in 6 M KOH; **d** galvanostatic charge–discharge curves of Ni_2Co_1 DH@APC electrode at various current densities of 1, 2, 5, and 10 A g^{-1}; **e** the dependence of C_{sp} on scan rate for Ni–Co DHs prepared with different Ni:Co molar ratios; **f** Nyquist plots of Ni_2Co_1 DH@APC and Ni_2Co_1 DH electrodes recorded in the frequency range from 0.01 to 100 kHz

and collection of electrons in the electrode. The major limitation of pseudocapacitor electrode materials is their inferior long-term stability, particularly at higher current densities [41]. Cycle stability is another crucial factor for supercapacitor application [42]. The CVs and EIS of the Ni_2Co_1 DH@APC composite before and after 1000 cycles are shown in Fig. 7. The anodic current around 0.42 V decreases significantly, which means that $Co(OH)_2$ is more easily converted to be condensed and dehydrated than that of $Ni(OH)_2$ during the long-term test, thus leading to slower kinetic activity and decreased current density. This phenomenon further confirmed that the content of $Ni(OH)_2$ plays a crucial role in improving

Table 1 Comparison of specific capacitances of Ni/Co composites based on different carbon materials

Composite	Ni/Co content	Scan rate or current density	Specific capacitance F g^{-1}	Reference
$Ni(OH)_2$/RGO	–	10 A g^{-1}	1125	[35]
α-$Ni(OH)_2$/CNT	66 wt%	0.5 A g^{-1}	1144	[36]
GO/$Co(OH)_2$/chitosan	–	10 mV s^{-1}	402	[37]
Nicl-LDH/GNS	89.7 wt%	1 A g^{-1}	1255.8	[38]
$Co(OH)_2$/RGO/NiO	–	5 mV s^{-1}	1470	[30]
Ni–Co LDH	Ni/Co = 1:2	1 A g^{-1}	2184	[39]
Ni–Co DH/RGO	Ni/Co = 1:1	1 A g^{-1}	835	[40]
Ni–Co DH@APC	Ni/Co = 2:1	1 A g^{-1}	1519	This work

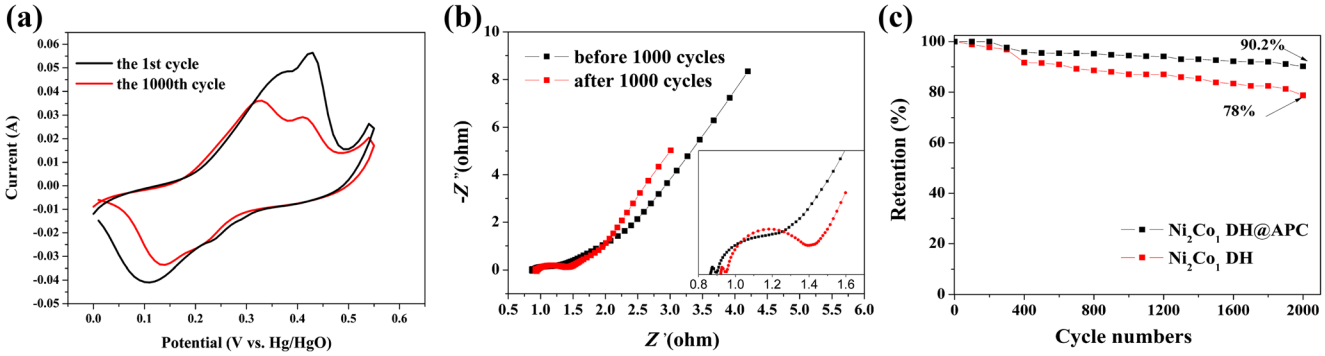

Fig. 7 **a** CV curves of Ni_2Co_1 DH@APC electrode before and after 1000 cycles at 5 mV^{-1}, **b** Nyquist plots of Ni_2Co_1 DH@APC electrode before and after 1000 cycles, and **c** charge/discharge test at a current density of 20 A g^{-1} for the Ni_2Co_1 DH@APC and Ni_2Co_1 DH electrodes

specific capacity. Figure 7b indicates the R_{ct} value of Ni_2Co_1 DH@APC tested after 1000 cycles only displays a little change. This may be attributed to the partial detachment of the active material from the nickel foam with an increase on contact resistance and Ni–Co DH particle size. The stability of Ni_2Co_1 DH@APC was also studied using galvanostatic charge–discharge with 2000 cycles at a high current density of 20 A g^{-1} (Fig. 7c). 90.2% of the C_{sp} value was retained even after 2000 cycles; however, that of Ni_2Co_1 DH without APC just remained 78%. This result clearly indicated that the APC was a better support and significantly improved the stability of the electrodes at a high current density.

To expand the application of electrodes, an ASC cell illustrated in Fig. 8a was assembled using as-prepared composite (Ni_2Co_1 DH@APC/nickel foam) as positive electrode and AC/nickel foam as negative electrode. Figure S5 presents CV curves of the positive and negative electrodes in a three-electrode system. The Ni_2Co_1 DH@APC (0–0.55 V) and AC (−1–0.2 V) offer a different potential range and indicate the combination could afford the cell a largely extended potential window, which is beneficial to improve the energy density of supercapacitors. Figure S6 shows the CV curves recorded at different potential windows for the ASC cell, in which the weight of positive and negative electrode was 1.6 and 1.7 mg,

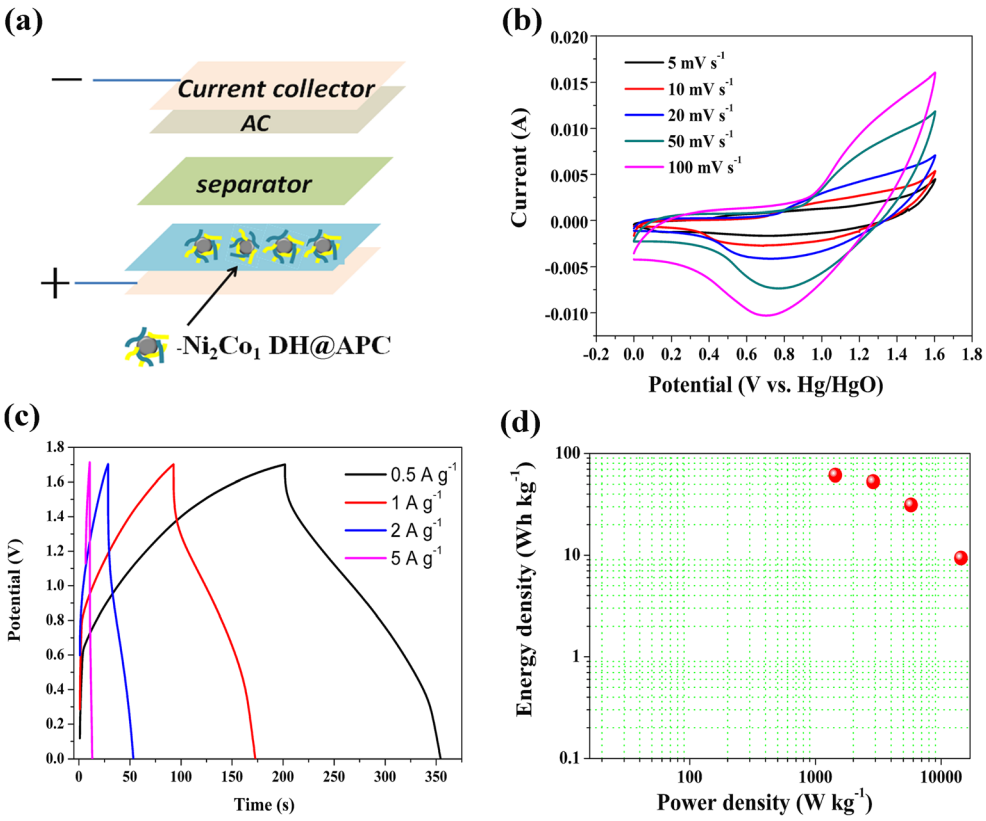

Fig. 8 **a** Schematic illustration of the ASC cell configuration, **b** CV curves of the ASC system recorded at different scan rates, **c** galvanostatic charge/discharge curves at different current densities, and **d** Ragone plot related to energy and power densities operated at 1.6 V

respectively. The stable electrochemical windows of the ASC system can be extended to 1.6 V. Moreover, galvanostatic charge–discharge curves of the ASC cell were tested within the potential window of 0–1.6 V. Figure 8b indicates typical CV curves of the ASC cell at different scan rates show similarity in shape and retain relatively rectangular shapes even at a scan rate of 50 mV s^{-1}, indicating high rate capability at fast charge and discharge. As shown in Fig. 8c, all the charge–discharge curves at different current densities generally show typical triangle-shaped curves, indicating well-balanced electrochemical reversibility at a relative high current density. The C_{sp} of the ASC at 0.5 A g^{-1} is calculated to be 47.8 F g^{-1}. The specific energy density (E) and specific power density (P) of the ASC cell can be calculated according to the charge–discharge curves in Fig. 8c and further converted into the Ragone plots, as shown in Fig. 8d. It exhibits a high energy density of 12 Wh kg^{-1} at a high power density of 14,400 W kg^{-1} at 5 A g^{-1}. In general, the participation of APC in the nanocomposite improves the electrical conductivity and dispersivity of active material. In addition, the supported Ni–Co DH nanowires possess a highly porous structure with more exposed active area and favorable surface modification. The synergistic mechanism further confirms the electrode based on APC assembled with Ni–Co DH nanowires has an excellent electrochemical performance and extensive potential in supercapacitor applications.

Conclusion

A biomass-derived porous carbon was obtained from apples through a simple hydrothermal carbonization. The results indicate the APC with a large surface area exhibits good conductivity, which is suitable as a support for NiCo double hydroxide nanowires. The Ni_2Co_1 DH@APC composite exhibits high specific capacitance, low charge transfer resistance, and superior capacitance retention because of its well-defined nanoporous structure and conductive network. Furthermore, the asymmetric supercapacitors exhibit a maximum energy density of 61.2 Wh kg^{-1}. The enhanced electrochemical performance can be ascribed to the synergistic effects, in which APC acts as an excellent support for dispersion and Ni–Co DH nanowires provide a conductive pathway for electron transport in redox reaction. This biomass-derived concept opens new research opportunities in identifying electrode materials from low-cost sustainable sources.

Acknowledgements This work is supported by the National Natural Science Foundation of China (NSFC, 21306119), the Chengdu Science and Technology Project (2015-HM01-00531-SF), the project of the Science and Technology Department in Sichuan province (17ZDYF1877), and the Outstanding Young Scientist Foundation of Sichuan University (2013SCU04A23).

References

1. Gao Y, Wu J, Zhang W, Tan Y, Gao J, Zhao J, Tang B (2014) The calcined zeolitic imidazolate framework-8 (ZIF-8) under different conditions as electrode for supercapacitor applications. J Solid State Electrochem 18(11):3203–3207
2. Yu C, Zhang L, Shi J, Zhao J, Gao J, Yan D (2008) A simple template-free strategy to synthesize nanoporous manganese and nickel oxides with narrow pore size distribution, and their electrochemical properties. Adv Funct Mater 18(10):1544–1554
3. Zhu T, Chen JS, Lou XW (2010) Shape-controlled synthesis of porous Co_3O_4 nanostructures for application in supercapacitors. J Mater Chem 20(33):7015–7020
4. Sun W, Rui X, Ulaganathan M, Madhavi S, Yan Q (2015) Few-layered $Ni(OH)_2$ nanosheets for high-performance supercapacitors. J Power Sources 295:323–328.5
5. Wu ZS, Wang DW, Ren W, Zhao J, Zhou G, Li F, Cheng HM (2010) Anchoring hydrous RuO_2 on graphene sheets for high-performance electrochemical capacitors. Adv Funct Mater 20(20):3595–3602
6. Ahn YR, Park CR, Jo SM, Kim DY (2007) Enhanced charge-discharge characteristics of RuO_2 supercapacitors on heat-treated TiO2 nanorods. Appl Phys Lett 90(12):122106–122106
7. Zhang J, Yu Y, Liu L, Wu Y (2013) Graphene–hollow PPy sphere 3D-nanoarchitecture with enhanced electrochemical performance. Nano 5(7):3052–3057
8. Sawangphruk M, Kaewsongpol T (2012) Direct electrodeposition and superior pseudocapacitive property of ultrahigh porous silver-incorporated polyaniline films. Mater Lett 87:142–145
9. Chen J, Xu J, Zhou S, Zhao N, Wong C-P (2016) Amorphous nanostructured FeOOH and Co–Ni double hydroxides for high-performance aqueous asymmetric supercapacitors. Nano Energy 21:145–153
10. Yang M, Choi BG (2016) Rapid one-step synthesis of conductive and porous MnO_2/graphene nanocomposite for high performance supercapacitors. J Electroanal Chem 776:134–138
11. Saravanakumar B, Purushothaman KK, Muralidharan G (2015) High performance supercapacitor based on carbon coated V_2O_5 nanorods. J Electroanal Chem 758:111–116
12. Wang Y, Zhang X, Li X, Li X, Zhao Y, Wei H, Liu Y, Jiang P, Liang M (2016) Highly dispersed ultrasmall $Ni(OH)_2$ aggregated particles on a conductive support as a supercapacitor electrode with superior performance. J Colloid Interface Sci 490:252–258
13. Tan P, Xiao T, Tan X, Xiang P, Jiang L, Wu D (2016) Facile preparation of 3D porous $Ni(OH)_2$/AC–Ni as high performance binder free electrode for supercapacitors. J Alloys Compd 656:714–719
14. Chen S, Duan J, Jaroniec M, Qiao SZ (2013) Hierarchically porous graphene-based hybrid electrodes with excellent electrochemical performance. J Mater Chem A 1(33):9409
15. Wu K, Liu Q (2016) Nitrogen-doped mesoporous carbons for high performance supercapacitors. Appl Surf Sci 379:132–13916
16. Sun Z, Hui L, Ran W, Lu Y, Jia D (2016) Facile synthesis of two-dimensional (2D) nanoporous NiO nanosheets from metal–organic frameworks with superior capacitive properties. New J Chem 40(2):1100–1103
17. Zhou G, Xiong T, He S, Li Y, Zhu Y, Hou H (2016) Asymmetric supercapacitor based on flexible TiC/CNF felt supported interwoven nickel-cobalt binary hydroxide nanosheets. J Power Sources 317:57–64
18. Chang L, Ren F, Zhao C, Xue X (2016) Synthesis of $Co(OH)_2$/$Ni(OH)_2$ nanomaterials with excellent pseudocapacitive behavior and high cycling stability for supercapacitors. J Electroanal Chem 778:110–11519

19. Zhang P, Gong Y, Wei Z, Wang J, Zhang Z, Li H, Dai S, Wang Y (2014) Updating biomass into functional carbon material in ionothermal manner. ACS Appl Mat Interfaces 6(15):12515–12522
20. Lotfabad EM, Ding J, Cui K, Kohandehghan A, Kalisvaart WP, Hazelton M, Mitlin D (2014) High-density sodium and lithium ion battery anodes from banana peels. ACS Nano 8(7):7115–7129
21. Wang R, Wang P, Yan X, Lang J, Peng C, Xue Q (2012) Promising porous carbon derived from celtuce leaves with outstanding supercapacitance and CO_2 capture performance. ACS Appl Mat Interfaces 4(11):5800–5806
22. Sun L, Tian C, Li M, Meng X, Wang L, Wang R, Yin J, Fu H (2013) From coconut shell to porous graphene-like nanosheets for high-power supercapacitors. J Mater Chem A 1(21):646223
23. Volfkovich YM, Bograchev DA, Rychagov AY, Sosenkin VE, Chaika MY (2015) Supercapacitors with carbon electrodes. Energy efficiency: modeling and experimental verification. J Solid State Electrochem 19(9):2771–2779
24. Jiang J, Chen H, Wang Z, Bao L, Qiang Y, Guan S, Chen J (2015) Nitrogen-doped hierarchical porous carbon microsphere through KOH activation for supercapacitors. J Colloid Interface Sci 452: 54–61
25. Jiang L, Yan J, Hao L, Xue R, Sun G, Yi B (2013) High rate performance activated carbons prepared from ginkgo shells for electrochemical supercapacitors. Carbon 56:146–154
26. Pu J, Li C, Tang L, Li T, Ling L, Zhang K, Xu Y, Li Q, Yao Y (2015) Impregnation assisted synthesis of 3D nitrogen-doped porous carbon with high capacitance. Carbon 94:650–660
27. Wu Q, Wen M, Chen S, Wu Q (2015) Lamellar-crossing-structured $Ni(OH)_2$/CNTs/$Ni(OH)_2$ nanocomposite for electrochemical supercapacitor materials. J Alloys Compd 646:990–997
28. Lo IH, Wang J-Y, Huang K-Y, Huang J-H, Kang WP (2016) Synthesis of $Ni(OH)_2$ nanoflakes on ZnO nanowires by pulse electrodeposition for high-performance supercapacitors. J Power Sources 308:29–36
29. Zheng X, Ye Y, Yang Q, Geng B, Zhang X (2016) Ultrafine nickel–copper carbonate hydroxide hierarchical nanowire networks for high-performance supercapacitor electrodes. Chem Eng J 290: 353–360
30. Xu H, Zhang C, Zhou W, Li GR (2015) $Co(OH)_2$/RGO/NiO sandwich-structured nanotube arrays with special surface and synergistic effects as high-performance positive electrodes for asymmetric supercapacitors. Nano 7(40):16932–16942
31. Zeng W, Zhang G, Wu X, Zhang K, Zhang H, Hou S, Li C, Wang T, Duan H (2015) Construction of hierarchical CoS nanowire@$NiCo_2S_4$ nanosheet arrays via one-step ion exchange for high-performance supercapacitors. J Mater Chem A 3(47): 24033–24040
32. Tang S, Sui L, Dai Z, Zhu Z, Huangfu H (2015) High supercapacitive performance of $Ni(OH)_2$/XC-72 composite prepared by microwave-assisted method. RSC Adv 5(54):43164–43171
33. Shang C, Dong S, Wang S, Xiao D, Han P, Wang X, Gu L, Cui G (2013) Coaxial $Ni_xCo_{2x}(OH)_{6-x}$/TiN nanotube arrays as supercapacitor electrodes. ACS Nano 7(6):5430–5436
34. Li J, Yang M, Wei J, Zhou Z (2012) Preparation and electrochemical performances of doughnut-like $Ni(OH)_2$–$Co(OH)_2$ composites as pseudocapacitor materials. Nano 4(15):4498
35. Zhang H, Zhang X, Zhang D, Sun X, Lin H, Wang C, Ma Y (2013) One-step electrophoretic deposition of reduced graphene oxide and $Ni(OH)_2$ composite films for controlled syntheses supercapacitor electrodes. J Phys Chem B 117(6):1616–1627
36. Wang L, Chen H, Cai F, Chen M (2014) Hierarchical carbon nanotube/α-Ni(OH)2 nanosheet composite paper with enhanced electrochemical capacitance. Mater Lett 115:168–171
37. Yin J, Lee HU, Park JY (2016) An electrodeposited graphite oxide/cobalt hydroxide/chitosan ternary composite on nickel foam as a cathode material for hybrid supercapacitors. RSC Adv 6(41): 34801–34808
38. Zhang L, Wang J, Zhu J, Zhang X, San Hui K, Hui KN (2013) 3D porous layered double hydroxides grown on graphene as advanced electrochemical pseudocapacitor materials. J Mater Chem A 1(32): 9046
39. Zheng X, Gu Z, Hu Q, Geng B, Zhang X (2015) Ultrathin porous nickel–cobalt hydroxide nanosheets for high-performance supercapacitor electrodes. RSC Adv 5(22):17007–17013
40. Subramani K, Lakshminarasimhan N, Kamaraj P, Sathish M (2016) Facile and scalable route to sheets-on-sheet mesoporous Ni–Co-hydroxide/reduced graphene oxide nanocomposites and their electrochemical and magnetic properties. RSC Adv 6(19):15941–15951
41. Wang X, Liu L, Wang X, Bai L, Wu H, Zhang X, Yi L, Chen Q (2010) Preparation and performances of carbon aerogel microspheres for the application of supercapacitor. J Solid State Electrochem 15(4):643–648
42. Iqbal N, Wang X, Ahmed Babar A, Yu J, Ding B (2016) Highly flexible $NiCo_2O_4$/CNTs doped carbon nanofibers for CO_2 adsorption and supercapacitor electrodes. J. Colloid Interface Sci 476:87–93